Plasmonic chirality of L-shaped nanostructure composed of two slices with different thickness

Yongkai Wang, Junchen Deng, Gang Wang, Tong Fu, Yu Qu, and Zhongyue Zhang[*]

School of Physics and Information Technology, Shaanxi Normal University, Xi'an 710062, China
[*]*zyzhang@snnu.edu.cn*

Abstract: A concise method is proposed to fabricate L-shaped Ag nanostructures (LSANs) for generating chirality. Prepared by glancing angle deposition, the LSAN composed of two slices with different thickness is stacked on self-assembled monolayer polystyrene nanosphere arrays by controlling substrate azimuth and deposition time. The strong optical chirality of LSANs is achieved in visible and near-IR regions by measurement. For the circular dichroism spectrum of LSANs, the intensity is enlarged, and its peaks red-shift with increasing thickness difference. When LSANs are stacked on polystyrene spheres of different diameters, enlargement and red-shift are also observed in their circular dichroism spectra with increasing thickness difference. The numerical calculations of finite element method show that the two slices composing LSAN provide cross-electric dipoles and their thickness difference provides phase difference for generating optical chirality. This study not only provides a concise and scalable method for fabricating chiral plasmonic nanostructures but also contributes to understand the knowledge of the mechanism of circular dichroism.

References and links

1. S. M. Kelly, T. M. Jess, and N. C. Price, "How to study proteins by circular dichroism," Biophysica Acta **1751**(2), 119–139 (2005).
2. M. Takezaki and Y. Kito, "Circular dichroism of rhodopsin and isorhodopsin," Nature **215**(5106), 1197–1199 (1967).
3. M. Hentschel, L. Wu, M. Schäferling, P. Bai, E. P. Li, and H. Giessen, "Optical properties of chiral three-dimensional plasmonic oligomers at the onset of charge-transfer plasmons," ACS Nano **6**(11), 10355–10365 (2012).
4. J. M. Slocik, A. O. Govorov, and R. R. Naik, "Plasmonic circular dichroism of Peptide-Functionalized Gold nanoparticles," Nano Lett. **11**(2), 701–705 (2011).
5. S. M. Swasey, N. Karimova, C. M. Aikens, D. E. Schultz, A. J. Simon, and E. G. Gwinn, "Chiral electronic transitions in fluorescent silver clusters stabilized by DNA," ACS Nano **8**(7), 6883–6892 (2014).
6. F. Zhu, X. Li, Y. Li, M. Yan, and S. Liu, "Enantioselective circular dichroism sensing of cysteine and glutathione with gold nanorods," Anal. Chem. **87**(1), 357–361 (2015).
7. F. Hidalgo and C. Noguez, "Optical activity of achiral ligand SCH3 adsorbed on achiral Ag55 clusters: relationship between adsorption site and circular dichroism," ACS Nano **7**(1), 513–521 (2013).
8. B. M. Maoz, R. van der Weegen, Z. Fan, A. O. Govorov, G. Ellestad, N. Berova, E. W. Meijer, and G. Markovich, "Plasmonic chiroptical response of silver nanoparticles interacting with chiral supramolecular assemblies," J. Am. Chem. Soc. **134**(42), 17807–17813 (2012).
9. W. Ma, H. Kuang, L. Xu, L. Ding, C. Xu, L. Wang, and N. A. Kotov, "Attomolar DNA detection with chiral nanorod assemblies," Nat. Commun. **4**, 2689 (2013).
10. Y. Mochida, H. Cabral, Y. Miura, F. Albertini, S. Fukushima, K. Osada, N. Nishiyama, and K. Kataoka, "Bundled assembly of helical nanostructures in polymeric micelles loaded with platinum drugs enhancing therapeutic efficiency against pancreatic tumor," ACS Nano **8**(7), 6724–6738 (2014).
11. J. B. Pendry, "A chiral route to negative refraction," Science **306**(5700), 1353–1355 (2004).
12. E. Plum, J. Zhou, J. Dong, V. A. Fedotov, T. Koschny, C. M. Soukoulis, and N. I. Zheludev, "Metamaterial with negative index due to chirality," Phys. Rev. B **79**(3), 035407 (2009).

13. J. K. Gansel, M. Thiel, M. S. Rill, M. Decker, K. Bade, V. Saile, G. von Freymann, S. Linden, and M. Wegener, "Gold helix photonic metamaterial as broadband circular polarizer," Science **325**(5947), 1513–1515 (2009).
14. J. Kaschke, J. K. Gansel, and M. Wegener, "On metamaterial circular polarizers based on metal N-helices," Opt. Express **20**(23), 26012–26020 (2012).
15. M. Decker, M. W. Klein, M. Wegener, and S. Linden, "Circular dichroism of planar chiral magnetic metamaterials," Opt. Lett. **32**(7), 856–858 (2007).
16. X. Yin, M. Schäferling, B. Metzger, and H. Giessen, "Interpreting chiral nanophotonic spectra: the plasmonic Born-Kuhn model," Nano Lett. **13**(12), 6238–6243 (2013).
17. M. D. Turner, G. E. Schröder-Turk, and M. Gu, "Fabrication and characterization of three-dimensional biomimetic chiral composites," Opt. Express **19**(10), 10001–10008 (2011).
18. J. K. Gansel, M. Latzel, A. Frolich, J. Kaschke, M. Thiel, and M. Wegener, "Tapered gold-helix metamaterials as improved circular polarizers," Appl. Phys. Lett. **100**(10), 101109 (2012).
19. R. Y. Wang, H. L. Wang, X. C. Wu, Y. L. Ji, P. Wang, Y. Qu, and T. S. Chung, "Chiral assembly of gold nanorods with collective plasmonic circular dichroism response," Soft Matter **7**(18), 8370–8375 (2011).
20. A. Kuzyk, R. Schreiber, Z. Fan, G. Pardatscher, E. M. Roller, A. Högele, F. C. Simmel, A. O. Govorov, and T. Liedl, "DNA-based self-assembly of chiral plasmonic nanostructures with tailored optical response," Nature **483**(7389), 311–314 (2012).
21. S. Eslami, J. G. Gibbs, Y. Rechkemmer, J. van Slageren, M. Alarcón-Correa, T.-C. Lee, A. G. Mark, G. L. J. A. Rikken, and P. Fischer, "Chiral nanomagnets," ACS Photonics **1**(11), 1231–1236 (2014).
22. B. Yeom, H. Zhang, H. Zhang, J. I. Park, K. Kim, A. O. Govorov, and N. A. Kotov, "Chiral plasmonic nanostructures on achiral nanopillars," Nano Lett. **13**(11), 5277–5283 (2013).
23. J. G. Gibbs, A. G. Mark, S. Eslami, and P. Fischer, "Plasmonic nanohelix metamaterials with tailorable giant circular dichroism," Appl. Phys. Lett. **103**(21), 213101 (2013).
24. A. G. Mark, J. G. Gibbs, T. C. Lee, and P. Fischer, "Hybrid nanocolloids with programmed three-dimensional shape and material composition," Nat. Mater. **12**(9), 802–807 (2013).
25. J. W. Leem and J. S. Yu, "Glancing angle deposited ITO films for efficiency enhancement of a-Si:H/ c-Si:H tandem thin film solar cells," Opt. Express **19**(103), 258–268 (2011).
26. H. Y. Yang, M. F. Lee, C. H. Huang, Y. S. Lo, Y. J. Chen, and M. S. Wong, "Glancing angle deposited titania films for dye-sensitized solar cells," Thin Solid Films **518**(5), 1590–1594 (2009).
27. N. Zhang, X. Su, P. Free, X. Zhou, K. G. Neoh, J. Teng, and W. Knoll, "Plasmonic metal nanostructure array by glancing angle deposition for biosensing application," Sens. Actuators B Chem. **183**, 310–318 (2013).
28. K. M. Krause and M. J. Brett, "Spatially graded nanostructured chiral films as tunable circular polarizers," Adv. Funct. Mater. **18**(20), 3111–3118 (2008).
29. J. H. Singh, G. Nair, A. Ghosh, and A. Ghosh, "Wafer scale fabrication of porous three-dimensional plasmonic metamaterials for the visible region: chiral and beyond," Nanoscale **5**(16), 7224–7228 (2013).
30. A. G. Dirks and H. J. Leamy, "Columnar microstructure in vapor-deposited thin films," Thin Solid Films **47**(3), 219–233 (1977).
31. G. K. Larsen, Y. He, W. Ingram, E. T. LaPaquette, J. Wang, and Y. Zhao, "The fabrication of three-dimensional plasmonic chiral structures by dynamic shadowing growth," Nanoscale **6**(16), 9467–9476 (2014).
32. K. Y. Ko, K. N. Lee, Y. K. Lee, and Y. R. Do, "Enhanced light extraction from SrGa2S4: Eu2+ film phosphors coated with various sizes of polystyrene nanosphere monolayers," J. Phys. Chem. C **112**(20), 7594–7598 (2008).
33. N. J. Greenfield, "Using circular dichroism spectra to estimate protein secondary structure," Nat. Protoc. **1**(6), 2876–2890 (2007).
34. P. B. Johnson and R. W. Christy, "Optical constants of the noble metals," Phys. Rev. B **6**(12), 4370–4379 (1972).
35. A. B. Pawar and I. Kretzschmar, "Patchy particles by glancing angle deposition," Langmuir **24**(2), 355–358 (2008).
36. X. Wu, J. Wang, and J. Y. Chen, "The effect of aspect ratio of gold nanorods on cell imaging with two-photon excitation," Plasmonics **8**(2), 685–691 (2013).
37. M. López-García, J. F. Galisteo-Lopez, C. Lopez, and A. Garcia-Martin, "Light confinement by two-dimensional arrays of dielectric spheres," Phys. Rev. B **85**(23), 235145 (2012).

1. Introduction

Chiral structures cannot be superposed with their mirror images. These structures present different optical response to left circularly polarized (LCP) and right circularly polarized (RCP) light, which is defined as circular dichroism (CD) [1,2]. Considering the strong interaction between light and noble metals, artificial chiral plasmonic nanostructures (ACPN) show stronger CD than chiral biomolecules [3–5]. Researchers deem that the generation mechanism of CD for ACPN is due to the couple of electric dipole moments and magnetic dipole moments [4,5]. ACPNs have been widely applied in analytical chemistry [6–8], biological monitoring [9,10], negative refractive index media [11,12], and broadband circular

polarization [13,14]. A simple, flexible, and effective method to fabricate ACPNs is needed to expand the application of ACPNs.

In recent years, four main methods have been used to fabricate ACPNs. First, electron beam lithography (EBL) was used to prepare planar ACPNs with precise dimensions [15,16]. For example, double-layer gammadion structure fabricated by EBL exhibits a pronounced CD in infrared. The antisymmetric oscillation modes of the two coupled layers exert larger effects on CD than similar single-layer systems. Second, direct laser writing method is used to fabricate 3D ACPNs in micrometer size [17,18]. Tapered gold-helix metamaterial fabricated by direct laser writing shows a bandwidth chiral that acts as circular polarizers [18]. Third, molecular self-assembly method is successfully used to helically assemble ACPNs in solutions [19,20]. DNA origami gold nanoparticle helices fabricated by molecular self-assembly method exhibit well-defined CD signatures in visible region [20]. Fourth, glancing angle deposition (GLAD) is used to prepare ACPNs in macroscopic area [21–24]. Chiral plasmonic nanostructures on achiral nanopillars fabricated by GLAD show strong and tunable chiroptical responses [22]. Furthermore, hybrid nanocolloids with anisotropic 3D shapes and material composition fabricated by Fischer group also show strong chirality [24]. Based on the abovementioned studies, the EBL method is complex, expensive, and limited by large-scale applications. Direct laser writing fabricates nanostructures with difficulty because of low resolution. Metal nanostructures fabricated by molecular self-assembly generally show weak chiral response because of processing in solutions. GLAD is deemed as an excellent method to fabricate ACPNs because of its scalability and conciseness.

By changing substrate azimuth and deposition time, GLAD can concisely fabricate scalable nanostructures for application in solar cells [25–27], ultrasensitive hydrogen sensor [27], and the preparation of helical nanostructures [28,29]. The main mechanism of GLAD is the geometric shadowing effect, which means that the evaporated material cannot be deposited on shadow areas in the vaporing direction [30,31]. The periodic nanotemplates are always used for providing periodic shadows. Self-assembled microsphere monolayer can be used as a simple template to form larger spectral windows.

In this paper, we prepared a concise and scalable monolayer chiral plasmonic nanostructure with different thicknesses on polystyrene (PS) nanosphere templates by GLAD. LSAN composed of two slices with different thickness are formed through rotating substrate azimuth and controlling deposited time. Experimental results show strong optical chirality of LSAN in visible and near-IR regions. With increasing thickness difference of LSAN, the intensity of CD spectrum is enlarged, and the peaks of CD spectrum red-shift. For PS spheres of different diameters, a similar characteristic is acquired. The trend of simulated results is consistent with experimental results. The distributions of charge density show that the two slices composing LSAN provide cross-electric dipoles and the different positions of the two-slice optical phase variation for generating optical chirality.

2. Methodology and simulation

2.1 Self-assembly of monolayer polystyrene nanosphere

The self-assembly PS nanospheres were prepared using the method in reference [32]. In particular, the preparation of self-assembly monolayer PS nanospheres includes six steps as shown in the Fig. 1. We initially used a sliced glass to separate the culture dish into left and right parts (A and B) where deionized water can go through from the bottom of the sliced glass. A glass block whose height is slightly lower than the sliced glass is placed into I part of culture dish. Then deionized water is filled until the level of deionized water reaching the height of the block glass. The mix solution PS nanosphere solution (6wt%) with ethyl alcohol according to specific proportions is slowly dripped on the surface of the glass block until the bluish violet monolayer PS nanosphere film overspreading the part I of the culture dish. The monolayer PS nanosphere film is pushed into a tight whole piece by the injector adhered TX-

100 solution (Polyethylene glycol tert-octylphenyl ether). Deionized water is filled until the level of deionized water slightly higher the level of the glass block. The monolayer PS nanosphere film is pushed to part II of culture dish by the injector adhering TX-100 solution. The sediment PS nanosphere below the monolayer PS nanosphere film is drawn by a injector. The monolayer PS nanosphere film is lifted using glass substrates disposed by Piranha solution.
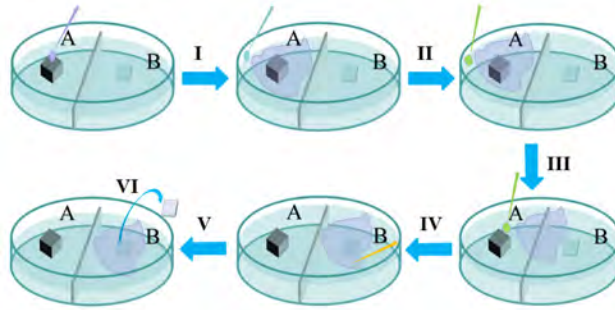

Fig. 1. The Schematics of self-assembly of PS monolayer. The process includes six steps: I droping PS solution, II injecting deionized water, III injecting TX100, IV pushing PS film, V drawing out sediment, and VI lifting glass substrate.

2.2 Characterization

An E-beam evaporator, DE 400 (DE Technology Inc), was used to deposit Ag layers on the monolayer PS nanosphere film. During whole deposition, chamber pressure was around 1×10^{-7} torr. The Ag slug is purchased from Alfa Aesar, 99.99% purity. Scanning electron microscope (SEM) and transmission electron microscope (TEM) images of all LSAN were obtained with a FEI Nova system and a JEM-2100 (JEOL), respectively. CD and UV−vis spectra were obtained with a Chirascan (Applied Photophysics Ltd) [33] and a Lambd 950 (Perkin-Elmer) at room temperature, respectively.

2.3 Simulation

The three-dimensional Maxwell's equations incorporating of R-LSAN are calculated using the finite element method (radio frequency model of COMSOL Multiphysics). The refractive index of air is regarded as 1. The frequency dependent permittivities of silver are referred from the Ref [34]. Due to slice fabricated by GLAD, the growing direction of slices has the about 30° angle with respect to the direction of substrate plane. For simplification, the increase of slices is regarded as a linear increase with the increase of vapor time. Here, the R-LSAN is composed by two different right parallelepipeds. At the six sides of the hexagonal unit cell, periodic boundary condition is assumed to obtain the optical response of monolayer R-LSAN on the hexagonal PS nanosphere arrays. Circularly polarized light, the wavelength range from 300 to 900 nm, normally irradiates on the unit cell by setting Ports in the COMSOL Multiphysics. The Perfectly Matched Layers are set up for absorbing light which pass through the Ports.

3. Results and discussion

3.1 Fabrication of LSAN

The fabrication process of LSANs starts with the preparation of self-assembled monolayer PS nanosphere arrays on glass substrates. Three templates are prepared by using spheres with different diameters, namely, $d = 380$, 280, and 180 nm, respectively. Two-step depositions are needed for deposition right-helical LSAN (R-LSAN) on PS nanospheres, as shown in Fig. 2. Here, φ is defined as the angle of substrate azimuthal orientation. In the first step, Ag is

deposited onto the monolayer at fixed oblique angle of $\theta = 86°$ with respect to z-axis. In the second step, the substrate is anticlockwise rotated at an angle of $\Delta\varphi = 90°$. Accordingly, for the left-helical LSAN (L-LSAN), the substrate is rotated clockwise at an angle of $\Delta\varphi = 90°$. The thicknesses of two-step depositions are setted as T_a and T_b in E-beam evaporator. To retain the morphology of LSAN on the different diameters of nanospheres, T_a and T_b are proportionately decreased according to the decrease in nanosphere diameters, d, as follows: to $d = 380$ nm, taking $T_a = 100$ nm, $T_b = 150, 200, 250$ nm; to $d = 280$ nm, taking $T_a = 70$ nm, $T_b = 105, 140, 175$ nm; and to $d = 180$ nm, taking $T_a = 50$ nm, $T_b = 75, 100, 150$ nm, respectively.
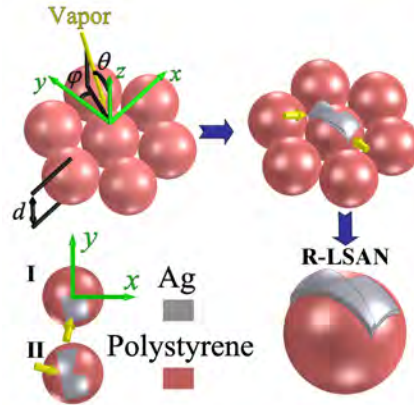

Fig. 2. Schematics of deposition process for R-LSAN. The process includes two steps: I and II as shown at the upper right. The direction of each deposition is indicated by the yellow arrow. Top-view figures of R-LSAN at each step are shown at the lower left. The deposited directions of the second step are rotated clockwise from the top view.

R-LSAN obtained by the above process is polycrystalline because of the template of hexagonal close-packed (HCP) PS nanospheres. Figure 3(a) shows a representative top-view SEM image of R-LSAN on PS nanosphere monolayer. The directions (black arrow) and the thickness of Ag deposition are indicated below in Fig. 3. Six distinct domains are marked as D_1, D_2, D_3, D_4, D_5, and D_6. Meanwhile, their higher-magnification SEM images are shown in Figs. 3(b-g), respectively. To illustrate the mechanism for forming different domains, we define each domain by using the azimuthal angle φ for the first Ag deposition. The initial φ can be degenerated as $\varphi = \varphi_0 + n\cdot60°$ because of the symmetry of the HCP lattice for $0° \leq \varphi_0 <$

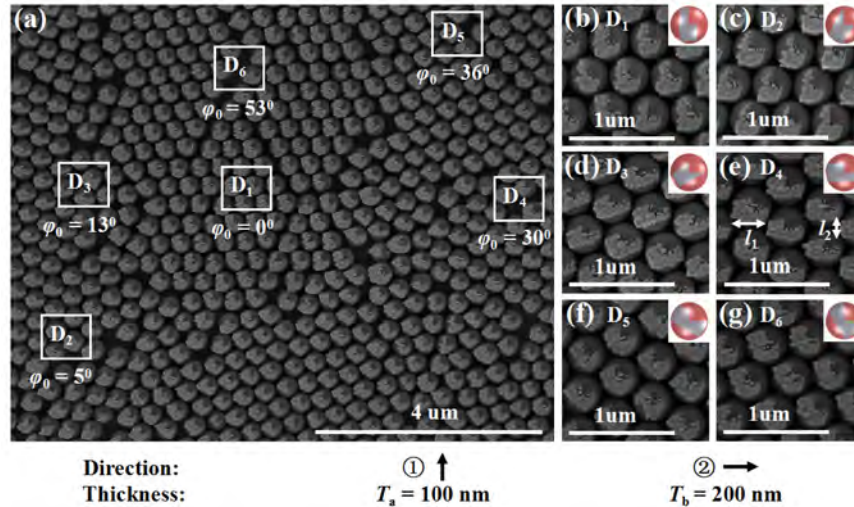Fig. 3. (a) Top-view SEM images of R-LSANs on d = 380 nm nanosphere monolayers, (b to d) higher-magnification images for domain D_1, D_2, D_3, D_4, D_5, and D_6, respectively. Insets are the schematic morphologies. The sequence and directions of depositions are shown at the bottom of the picture.

60°, where n is an integer. In this paper, φ_0 refers to the initial azimuthal angle to define different domains. As shown in Fig. 3, for domains D_1-D_6, φ_0 = 0°, 5°, 13°, 30°, 36°, 53°, respectively. The morphology of a single Ag slice is influenced by φ_0 [35]. The SEM images verify the influence, as shown in Figs. 3(b-g). At φ_0 = 30°, the dimensions of individual patches are respectively marked by l_1 and l_2, as shown in Fig. 3(e). The measured l_1 and l_2
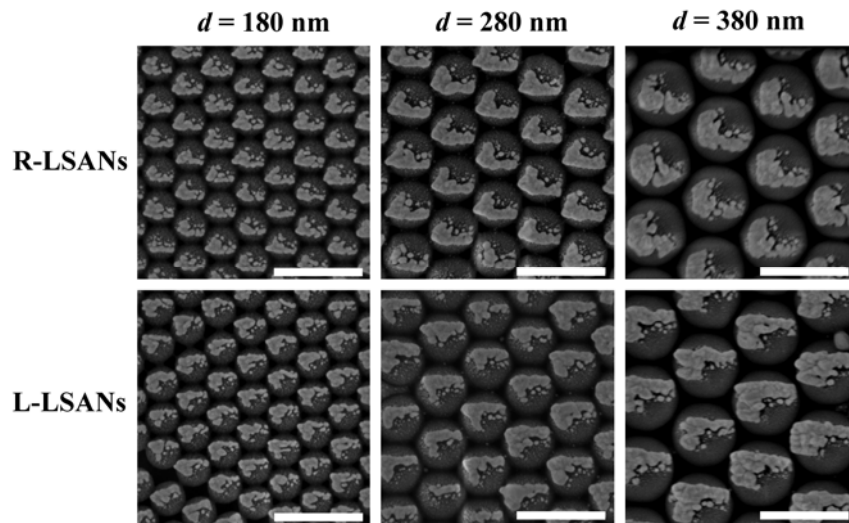

Fig. 4. For φ_0 = 30°, top-view SEM images of R- and L-LSANs on the PS monolayers of d = 180, 280, and 380 nm, respectively. The scale bar in each image is unified as 500 nm.

values of R-LSAN on PS nanospheres with different d values are listed in Tab. 1. The aspect ratio of l_2/l_1 slightly enlarges as d increases. Similar domain areas for Figs. 3(b-g) were found to be mostly distributed between 10 and 100 μm^2, indicating that the PS domain of prefect orientation is nonexistent. Therefore, individual LSAN presents anisotropic structures for each domain, but the array of LSAN domains is isotropic on the macroscale corresponding to

the dimension of the optical beam. Figure 4 shows the SEM images of R- and L-LSANs on the PS monolayers of d = 180, 280, and 380 nm, respectively. The SEM images of R- and L-LSANs are in mirror symmetry.

Table 1. Structural Parameters of R-LSAN on the Nanosphere of Different Diameter d

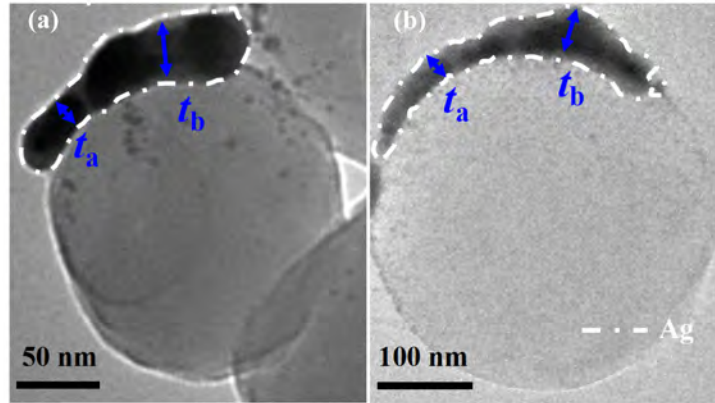|	d = 180 nm	d = 280 nm	d = 380 nm
T_a (nm)	50	70	100
T_b (nm)	100	140	200
l_1 (nm)	173 ± 10	244 ± 10	335 ± 10
l_2 (nm)	104 ± 10	168 ± 10	220 ± 10
aspect ratio, l_2/l_1	0.60 ± 0.06	0.65 ± 0.04	0.67 ± 0.03

Fig. 5. TEM images of R-LSANs cross-sections (a) for d = 180 nm, T_a = 50 nm, and T_b = 100 nm; (b) for d = 380 nm, T_a = 100 nm, and T_b = 200 nm corresponding to actual thicknesses, t_a = 20 nm and t_b = 40 nm (marked using blue arrows), respectively. The encircled areas by white dashed lines indicate the artificially deposited Ag slices.

To measure the thickness of LSAN, we use TEM to represent the cross-sections of LSAN. The TEM image of R-LSAN on the nanosphere of d = 180 nm is shown in Fig. 5(a), with T_a = 50 nm and T_b = 100 nm. Evidently, Ag appears to be considerably darker than PS because of a larger scattering cross-section for Ag. The white dashed lines are artificially added to better present the stacked Ag slices. The similar TEM image of R-LSAN on the nanosphere of d = 380 nm is shown in Fig. 5(b) with T_a = 100 nm and T_b = 200 nm. The actual thickness is different with the deposited nominal thickness setted in the E-beam evaporator. For the PS d = 380 nm, when the nominal deposited thicknesses are T_a = 100 nm and T_b = 200 nm, the actual thicknesses of Ag slices are approximately t_a = 20 nm and t_b = 40 nm.

3.2 Characterization of experimental spectra

Unpolarized ultraviolet-visible spectrophotometer is used to obtain the unpolarized transmittance spectra of LSANs. The unpolarized transmittance spectra of LSANs strongly rely on diameter d, but without optical chirality, as shown in Fig. 6(a). In the transmittance spectra, a broad valley appears at around λ = 500 nm for d = 180 nm, corresponding to the localized surface plasmon resonance (LSPR) of Ag layers. With d increasing to 280 and 380 nm, this valley becomes broader and red-shifts to λ = 600, 755 nm, respectively. Solid arrows are used to mark these transmittance valleys in Fig. 6(a). In theory, with the increase of T_a and T_b along the wave vector direction, the positions of LSPRs of metal nanoparticles are blue-shifted because of the decrease aspect ratio; with increasing d along the direction of polarization, the LSPR of metal nanoparticles is red-shifted because of increasing aspect ratio [36]. In this section, an evident red shift is observed with the increase of T_a, T_b, and d. Hence, the influence of d is stronger than the influence of T_a and T_b on the unpolarized transmittance spectra of LSANs. For LSANs on the PS nanosphere monolayers of d = 280 and 380 nm, the

transmittance valleys at 380, 520 nm are due to first diffracted order, respectively [37]. The valleys also appear in the transmittance spectra of PS monolayers and are marked by dashed arrows and "PS" in Fig. 6(a).
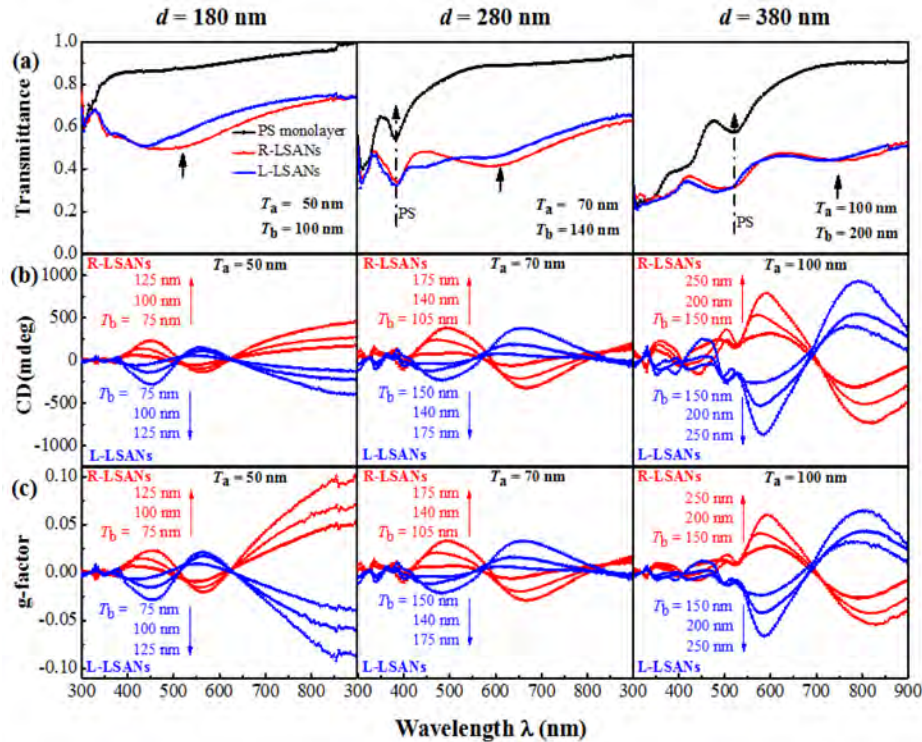

Fig. 6. For the different nanospheres of d = 180, 280, 380 nm: (a) Unpolarized transmittance spectra, (b) CD spectra, and (c) g-factor of LSANs with different T_a and T_b, respectively. Note that black dash arrows (PS) and black solid arrows in (a) mark the wavelength locations for first diffracted order of PS nanospheres and the LSPR of LSANs, respectively.

To obtain the chiral optical properties of LSANs, we measured CD (mdeg) spectra by Chirascan. As shown in Fig. 6(b), R-LSAN and L-LSAN present mirrored CD response from λ = 300 nm to λ = 900 nm. For both R-LSAN and L-LSAN on nanospheres of d = 180 nm, the intensity of CD spectra are enlarged and CD spectra are red-shifted with increasing T_b. For R-LSAN, broad valleys in the range from 500 nm to 620 nm indicate that the absorption of LCP light is smaller than the absorption of RCP light. The intensity of CD signal for R-LSAN is enlarged from −58 mdeg to −142 mdeg, or by 2.4 times, with the varied T_b from 75 nm to 125 nm. For L-LSAN, the intensity is magnified from + 56 mdeg to + 148 mdeg, or by 2.6 times, with the same change in T_b. The same trend of enlargement and red-shift also exist in d = 280, 380 nm with increasing T_b. As d increases to 280 and 380 nm, the position of CD valley red-shifts to around 660 and 820 nm, respectively, for respective maximal T_b. Meanwhile, the maximal magnitude of the CD valley for R-LSAN is magnified to −330 and −740 mdeg, respectively. We measured the CD spectra of LSANs at different azimuthal orientations of substrates and CD spectra under front and back illumination. The CD responses at longer wavelength (600 nm – 900 nm) do not depend on the azimuthal orientation angle and irradiation direction obviously, which reveals the weak linear birefringence and polarization conversion of LSANs.

In addition, the asymmetry g-factor is defined as $g = \Delta A / A$, where ΔA = CD (mdeg) / 33000 is the difference of absorption between LCP and RCP light, and A is the unpolarized absorption of LSAN. For the different nanospheres, Fig. 6(c) shows g-factor of LSANs with

different T_a and T_b. The characteristics of enlargement and red-shift are similar with the CD spectra. The g-factor of the corresponding LSAN reaches up to −0.054 for R-LSAN and + 0.064 for L-LSAN around the peak. In this section, the intensity of the g-factor of the LSAN is higher than the plasmonic optical activity in the visible range as observed in recent studies [29]. Notably, the typical order of the magnitude of g-factors is below 10^{-3} in most cases [29]. The higher g-factor is achieved merely by the conciseness of the plasmonic nanostructure of the thickness difference on PS nanosphere templates by GLAD.
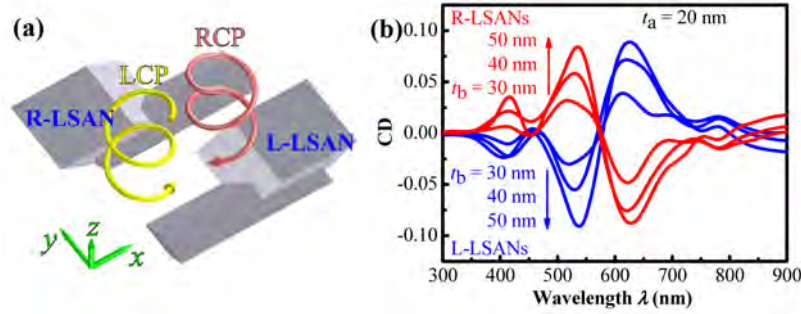
3.3 Analysis of simulation

Fig. 7. Computational simulation of the optical behavior of LSANs on nanospheres of $d = 380$ nm. (a) Geometric models of L- and R-LSAN. (b) Calculated CD = A_L-A_R spectra of LSANs with the different t_b and fixed $t_a = 20$ nm.

To confirm the attribution of LSAN to CD effects, simplified models are simulated by finite element method (radio frequency model of COMSOL Multiphysics). For every slice fabricated by GLAD, the growth direction of increased T_b shows about 30° between the substrate plane. Figure 7(a) shows the geometric models of R-LSAN and L-LSAN on $d = 380$ nm monolayers, which are simply composed by two right parallelepipeds that intersect at 30° with respect to xy plane. Given that LSAN fabricated by glancing deposition, the nominal deposition thicknesses (T_a and T_b) in the experiment are different from the actual deposition thicknesses. The actual deposition thicknesses are $t_a = 20$ nm, $t_b = 30, 40, 50$ nm, accordingly. The lengths of right parallelepipeds are defined by $l_1 = 335$ nm and $l_2 = 220$ nm, respectively. In Fig. 7(b), the CD spectra of R-SAN and L-LSAN with different t_b and fixed $\varphi_0 = 30°$ are shown under normal incidence of circularly polarized light. With the increase of t_b, the enlargement and red-shift of simulated spectra agree with the measured spectra in Fig. 6(b) for $d = 380$ nm. For fixing t_b, the simulated spectra are blue-shifted in comparison with the experimentally observed spectra. It is due to the decrease in electronic resonance length on the plasmonic structure, when we simply approximated plane slices from cambered slices on the nanospheres in the experiment. Meanwhile, the spectra are more fluctuant than the experimentally observed spectra because of the average effect in the experiment.
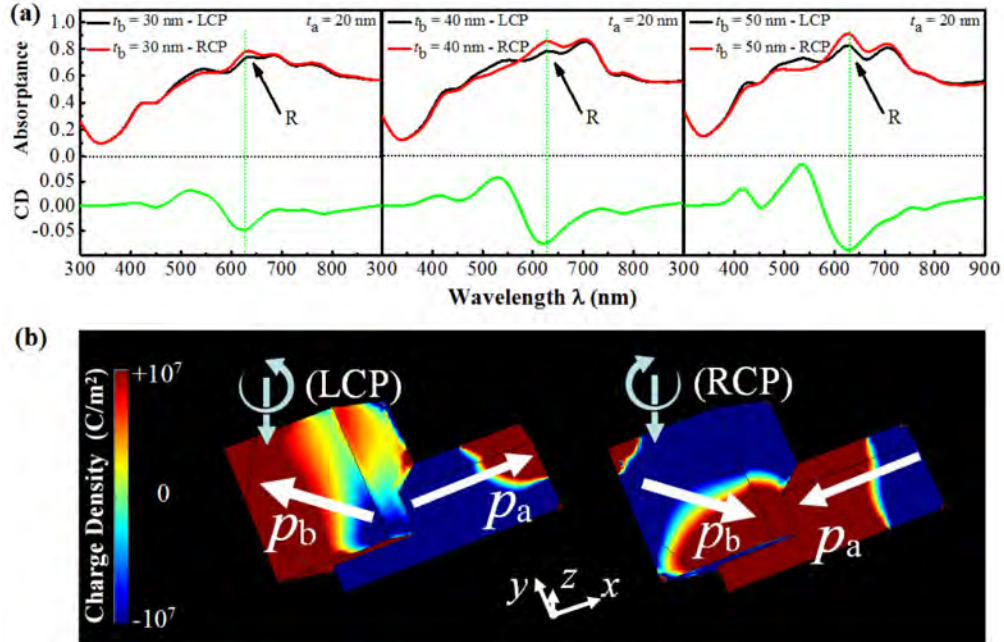
Fig. 8. (a) The simulated circular polarized absorptance and CD spectra of R-LSANs for $d = 380$ nm, $t_a = 20$ nm, and $t_b = 30, 40, 50$ nm, respectively. (b) The near-field distributions of charge density (rainbow) for $t_a = 20$ nm and $t_b = 40$ nm at the resonant wavelength marked "R". Equivalent electric dipole moments are marked by white arrows and labeled by "p_a" and "p_b", which is located at the two slices of different thicknesses t_a and t_b, respectively.

The mechanism of generating CD is explained by the Born–Kuhn oscillator model, which consists of two identical nanorods displaced vertically [16]. For right-hand structures, bonding mode is more easily excited by LCP light than RCP light. Conversely, anti-bonding mode is more easily excited by RCP light than LCP light [16]. When the distance between the two nanorods is shorter than an effective quarter wavelength, RCP light excited not only bonding mode but also anti-bonding mode. The simplest plasmonic version of Born–Kuhn configuration shows the fundamental optical chiral activity with bonding mode and antibonding mode. To illustrate the enlargement and red-shift of the CD spectra of R-LSAN with the increase of t_b, we show the absorptance spectra under LCP and RCP light and CD with fixed $t_a = 20$ nm varied t_b from 30 nm to 50 nm in Fig. 8(a). In the CD spectrum, apparent dips are observed at $\lambda = 620, 625, 630$ nm with increasing t_b. The positions of dips in the CD spectra correspond to the positions of peaks in the absorptance spectra, which indicate electronic resonances on R-LSAN. The resonant peaks labeled as "R" in absorptance spectra are red-shifted with the increased t_b, which leads to the red-shift of the dip in the CD spectra. The near-field COMSOL simulations at these wavelengths reveal that these resonances present similar near-field distributions of charge density. The distributions of charge density for $t_b = 40$ nm are shown in Fig. 8(b). Equivalent electric dipole moment are marked by white arrows and labeled by "p_a" and "p_b", which are located on two slices of different thicknesses. The two slices provide crossed p_a and p_b for forming an anti-bonding mode, and the different thicknesses of the two slices in the direction of the wave vector provide phase difference. Thus, resonant mode R in absorptance spectra can be regarded as the Born–Kuhn model for the CD effect. For R-LSAN, the anti-bonding mode is not only excited by RCP light but also by LCP light at the position of resonance "R". In this case, the polarization vector of the light does not fully align with the lower slices. However, the anti-bonding mode is effectively still excited by RCP light because of its preferred symmetry for RCP light, which generates

optical chirality. The red-shift of resonance "R" is due to the increasing resonant distance of p_b with increasing t_b. The enlargement of CD is due to the increasing resonant areas of electric dipoles p_b with increasing t_b. In addition, with the replacement of Ag with Si, the intensity of CD is reduced, and the dip width of the CD spectrum becomes broader. The result demonstrates that the plasmonic property of Ag performs an important function in achieving chiroptical response.

4. Concluding remarks

In summary, we propose a concise method of fabricating monolayer chiral plasmonic nanostructure. By controlling substrate azimuth and deposition time of glancing angle deposition, LSAN comprising two slices with different thickness are stacked on self-assembled monolayer PS nanosphere arrays, which forms a thickness difference along two azimuthal orientations. Experimental results show that the intensity of CD spectra of LSAN are enlarged and the CD spectra are red-shift with increasing thickness difference of two slices for LSAN on the PS spheres of different diameters. Numerical calculations show that the two slices comprising LSAN provide cross-electric dipoles, and the different thicknesses positions of the two slices provide phase difference for generating optical chirality. This study not only provides a concise and scalable method for fabricating chiral plasmonic nanostructures but also contributes to the understanding of the mechanism of chirality generation.

Acknowledgments